Journal of Materials Processing Tech. 259 (2018) 58–67

Contents lists available at ScienceDirect

Journal of Materials Processing Tech.

journal homepage: www.elsevier.com/locate/jmatprotec

Microstructure and mechanical properties of laser welded dissimilar joints between QP and boron alloyed martensitic steels

Qiang Jia[a,b], Wei Guo[b,*], Zhandong Wan[b], Yun Peng[c], Guisheng Zou[a,*], Zhiling Tian[c], Y. Norman Zhou[d]

[a] Department of Mechanical Engineering, Tsinghua University, Beijing, 100084, China
[b] School of Mechanical Engineering and Automation, Beihang University, Beijing, 100191, China
[c] Welding Research Institute, Central Iron and Steel Research Institute, Beijing, 100081, China
[d] Department of Mechanical and Mechatronics Engineering, University of Waterloo, Waterloo, Ontario, N2L 3G1, Canada

ARTICLE INFO

Keywords:
Quenching and partitioning steel
Hot stamping boron steel
Laser welding
Retained austenite
Mechanical properties

ABSTRACT

The newly developed quenching and partitioning (QP) steel QP980 and boron alloyed martensitic steel B1500HS were butt-welded using fiber laser at a constant laser power 4.5 kW and various welding speeds of 4 ~ 10 m/min. Retained austenite was measured in the super-critical HAZ of B1500HS (0.9%), inter-critical HAZ of B1500HS (3.4%) and inter-critical HAZ of QP980 (0.6%), while the sub-critical HAZ of QP980 witnessed decomposition of retained austenite from 8.4% to 4.4%. The joints welded at 4 m/min achieved the highest tensile strength, while the significantly softened HAZ of the B1500HS was the weakest region. The dissimilar joint welded at 6 ~ 8 m/min fractured at the base metal of QP980, which were preferred as more crash energy can be absorbed. However, the Erichsen values of these welded joints (~ 4.06 mm) significantly decreased compared with the base metal of B1500HS (7.46 mm) and QP980 steel (8.67 mm), as the crack propagated along the softened HAZ of B1500HS.

1. Introduction

The last decade saw the rapid development of automotive industry, with an increasing requirement of crash safety and weight reduction. Advanced high strength steel (AHSS) is one of the promising solution to satisfy the need of automobile. The development of AHSS is aimed at an excellent combination of strength and ductility with lower price. A new heat treatment processing, “quenching and partitioning” (QP), based on stabilizing austenite via C partitioning from the pre-quenched martensite, was proposed by Speer et al. (2003) to develop the third generation of AHSS. As reported by Speer et al. (2005), the retained austenite (RA) in QP steel transformed into martensite during plastic deformation, allowing for enhancement of strength and ductility. QP steel therefore can be made into tailored blanks with excellent formability. Currently, researches in QP steel are oriented towards the heat treatment process, and the corresponding microstructure as well as the mechanical performance of the steel. However, there are few studies on welding of QP steel up to now. Wang et al. (2014) studied the tensile and fatigue behaviors of resistance spot welding (RSW) joints of QP980, and indicated that the failure mode of tensile test specimen was interfacial failure or pullout failure, and the cracks in HAZ initiated at the interface among the sheets during fatigue test. Dissimilar RSW of QP and twining induced plasticity (TWIP) steel sheets has been studied by Spena et al. (2016). And the results showed that the weld nuggets exhibited an austenitic microstructure and the joints predominantly failed at the TWIP side. It is still unclear about the microstructure evolution and change in mechanical behavior of QP steel after either laser similar welding of QP steel or dissimilar welding of QP steel to other kinds of AHSSs.

The hot stamping martensitic steel with ultra-high strength (i.e. over 1500 MPa) is playing an important role in safety-related parts of automobile industry, as described by Luo et al. (2016). It is promising to apply the newly developed QP steel and the hot stamping martensitic steel to body-in-white to achieve combination of the excellent mechanical properties. For example, the two steels can be used for door reinforcements, windshield frame upright reinforcements and so on. These two dissimilar steel sheets can be integrated together with different thickness by tailor welded blanks (TWBs) to fit particular application. However, the heat affected zone (HAZ) softening of the steels containing martensite after welding may degrade the mechanical properties of overall joint. Jong et al. (2011) investigated the microstructural changes and mechanical behavior of RSW Usibor 1500 steel, and found a dramatic decline in hardness in the HAZ due to the formation of tempered martensite and ferrite, which was approximately

* Corresponding authors.
E-mail addresses: gwei@buaa.edu.cn (W. Guo), zougsh@tsinghua.edu.cn (G. Zou).

https://doi.org/10.1016/j.jmatprotec.2018.04.020
Received 20 January 2018; Received in revised form 10 April 2018; Accepted 10 April 2018
Available online 14 April 2018
0924-0136/

Table 1
Chemical compositions (wt. %) and tensile properties of the BM.

Material	C	Mn	Si	Al	Cr	B	Mo	Fe	YS (MPa)	UTS (MPa)	Elongation (%)
QP980	0.20	2.41	1.31	0.06	0.04	–	–	Balance	687	1067	26.1%
B1500HS	0.28	1.26	0.31	0.08	0.14	0.03	0.25	Balance	1137	1587	6.1%

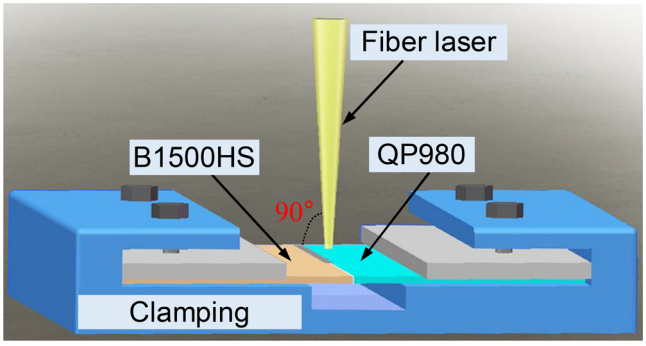

Fig. 1. Schematic diagram of laser welding.

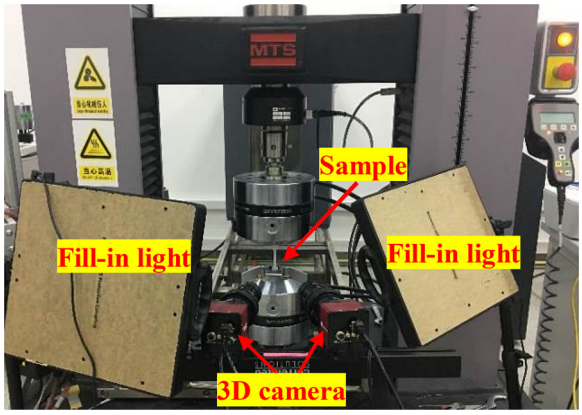

Fig. 2. Electromechanical universal testing machine equipped with DIC system.

230 Hv lower than that of base metal (BM). Wang et al. (2013) welded the 22MnB5 steel using tungsten inert gas arc welding process (TIG), and the joint obtained under the optimum heat input of 3840 J/cm showed the highest tensile strength for hot-dipped Al coating steel.

Among the various welding methods, laser welding has advantages due to its high energy density and quality, as demonstrated by Zhou et al. (2017). Previous studies on AHSS revealed that the fusion zone (FZ) usually contain martensite due to the high cooling rate during laser welding as well as the carbon and other alloying elements. For example, Gu et al., (2012) observed fully lath martensite in the FZ of ultra-high strength steel under various welding speeds. Researchers have discovered that laser welding under optimized process could provide narrow HAZ with improved mechanical properties compared with conventional arc welding processes, as reported by Lee et al. (2014). Němeček et al. (2012) reported that laser welded joint of transformation-induced plasticity (TRIP) steel failed in the BM during tensile test, indicating that the narrow HAZ had minimal effect on the overall mechanical properties of the joint. In this study, QP980 steel and hot stamping boron alloyed steel B1500HS were butt-welded using fiber laser welding under a constant laser power of 4.5 kW, with welding speeds ranged from 4 to 10 m/min. Microstructure evolution as well as the RA changes after laser welding were characterized. The influence of heat input on microhardness, tensile behavior and forming characteristic of the joint was investigated. Particular attention was paid to the strain distribution during tensile loading using digital image correlation (DIC).

2. Experimental procedures

1.36 mm thick QP980 steel sheet and 1.20 mm thick hot stamping boron alloyed steel sheet B1500HS provided by Baosteel were used in the experiments. Table 1 listed the chemical compositions and mechanical properties of the BM. The milling machined steel sheets (200 mm × 400 mm) were welded in butt-joint configuration, as shown in Fig. 1. Laser welding was conducted by an IPG Photonics YLS-6000 fiber laser system, with a focal length of 300 mm, a fiber core diameter of 0.3 mm and a laser beam spot diameter of 0.6 mm. The laser beam was perpendicular to the steel sheets to be welded, and no shielding gas was employed during laser welding. Different welding speeds from 4 to10 m/min were adopted at constant laser power 4.5 kW.

The laser welded joints were transversely cross sectioned, and then mechanically grounded, polished, followed by 4% nital solution to prepare metallographic samples. Optical microscope (OM, Olympus DP72), scanning electron microscope (SEM, Zeiss Sigma 500) and

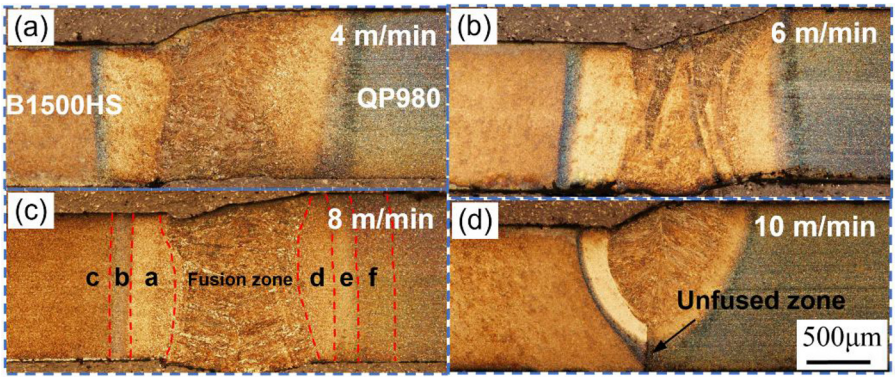

Fig. 3. Overview of the weld cross-section (where a, b and c represent super-critical HAZ, inter-critical HAZ and sub-critical HAZ of B1500HS, respectively; d, e and f represent super-critical HAZ, inter-critical HAZ and sub-critical HAZ of QP980, respectively).

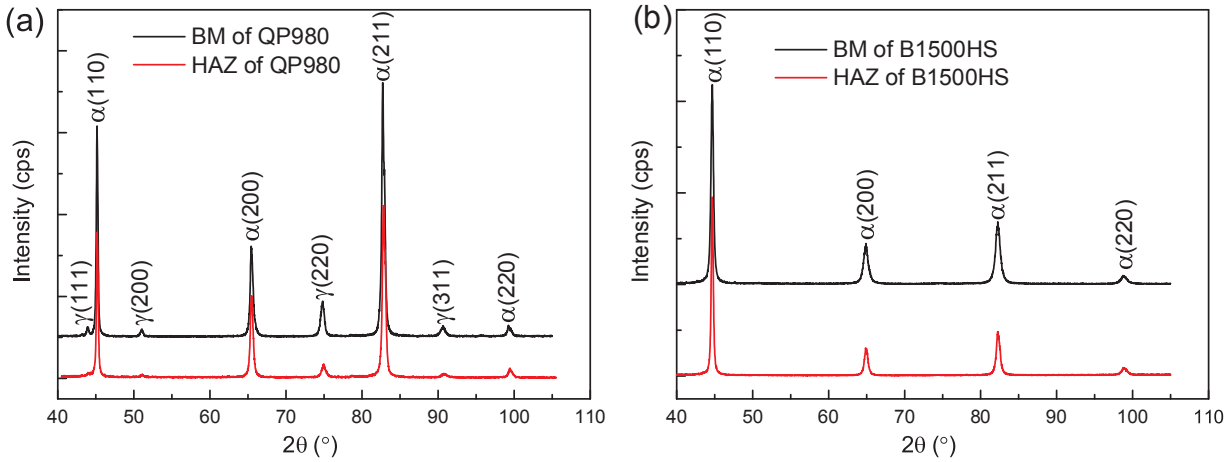

Fig. 4. XRD patterns of BM and HAZ: (a) QP980 and (b) B1500HS.

electron back-scattered diffraction (EBSD) were used to explore the microstructure.

Samples used for EBSD measurements were accurately polished by argon ion milling (Leica, 5.0 kV for 30 min, 4.5 kV for 30 min and 4.0 kV for 30 min). X-ray diffraction (XRD, Rigaku, Cu-Kα radiation, 40 kV, 150 mA) according to the integrated intensities of (200) $_{\alpha}$, (211) $_{\alpha}$, (200) $_{\gamma}$, (220) $_{\gamma}$ and (311) $_{\gamma}$ diffraction peaks was employed to measure the volume fraction of the RA. Samples for XRD measurement were electrolytically polished and stress relieved in a solution of 10% glycerin, 70% ethyl alcohol and 20% perchloric acid.

Microhardness across the welded joint was tested under a load of 300 g and 15 s dwell time using a Vickers hardness tester (FM 800). Flat tensile samples with a width of 6.0 mm and a gauge length of 25.0 mm were machined according to ASTM: E8M standard, and the tests were carried out by an electromechanical universal testing machine (MTS C45105) equipped with DIC (CSI VIC-3D) system with a constant speed of 1.5 mm/min, as shown in Fig. 2. Erichsen cupping test was carried out via universal sheet formability testing machine (BCS-30D) at a constant speed of 10 mm/min.

3. Results and discussion

3.1. Microstructure and hardness

Fig. 3 presents the cross-section images of the welded joints. It can be found that the dissimilar AHSSs were successfully butt-welded at the welding speeds of 4 ~ 8 m/min, while the joint exhibited an unfused zone at the welding speed of 10 m/min due to insufficient heat input. Other weld defects such as undercut were not found in the present study.

XRD diffraction patterns in Fig. 4 indicate that the BM QP980 steel contained both face centered cubic (FCC) γ and body centered cubic (BCC) α crystal structure, while the B1500HS only exhibited BCC crystal structure. Also, the volume fraction of approximately 10.86% RA (γ) was determined in the BM QP980. The SEM microstructures and EBSD orientation maps of BM are presented in Fig. 5a-b. The microstructure of QP980 was comprised of tempered martensite (TM) matrix with irregular-shaped blocks, untempered martensite, ferrite and RA. The grains in the QP980 presented some rolling texture. The B1500HS steel mainly consisted of fine-grained martensite with random texture. As shown in Fig. 5c, the FZ of the joint made with 8 m/min presented a typical microstructure of a laser weld, fully lath martensite. The FZ near the B1500HS side exhibited the highest hardness (~545 Hv), whereas the FZ near the QP980 side had lower hardness (~500 Hv), as illustrates in Fig. 6. This was because that the B1500HS steel had higher carbon content than did QP980 and that the FZ has not chemically homogenized due to fast solidification during laser welding.

The HAZ microstructure of B1500HS can be divided into three regions according to the peak temperatures it experienced during laser welding (Fig. 3). As shown in Fig. 7a, the super-critical HAZ was subjected to a peak temperature just above A_{c3}, thus allowing austenite to nucleate. Such austenite grains transformed into fine grain martensite during the subsequent cooling. This region possessed nearly the same hardness value as the FZ. The inter-critical HAZ went through a peak temperature between A_{c1} and A_{c3}, which thus was partially austenitized. Such austenite transformed into martensite or perhaps untransformed (i.e., retained austenite) during cooling. In this inter-critical HAZ, the prior ferrite was essentially unaffected. Therefore, the microstructure was made up of martensite, ferrite and a small amount of RA in this region as shown in Fig. 7b. The region in HAZ subjected to a peak temperature just below the lower critical temperature, A_{c1}, saw the martensite decomposition and the carbides precipitation, as indicates in Fig. 7c. Therefore, this subcritical HAZ significantly softened with the hardness dropped by 187 Hv (Fig. 6). The HAZ softening became more serious under high heat input. For example, the hardness of the softened HAZ declined to approximately 309 Hv at the welding speed of 4 m/min. This softened region may cause premature failure of the welded joint, as reported by Jia et al. (2017).

The HAZ of QP980 had similar microstructures to that of B1500HS in the super-critical HAZ and inter-critical HAZ, as shown in Fig. 7d-e. Softening phenomenon in the sub-critical HAZ of the QP980 was also observed. However, the hardness of the area only dropped by 15 Hv (seen in Fig. 6). As some martensite in the BM QP980 was already tempered during the manufacturing process of partitioning, only the part of untempered martensite, also referred as fresh martensite by de Diego-Calderon et al. (2015), decomposed during the laser welding, as can be found in Fig. 7f.

Coates (2014) reported that the hard martensite distributed in soft matrix of ferrite contributes to high work hardening rates, such as in dual phase (DP) steel. For the QP steel, the RA gradually transforms into martensite with increasing strain, resulting in higher work hardening rates at higher strain levels known as TRIP effect, as described by Nayak et al. (2012). The distribution of RA in QP steel presented various morphologies, as shown in the EBSD image in Fig. 8a. The RA was

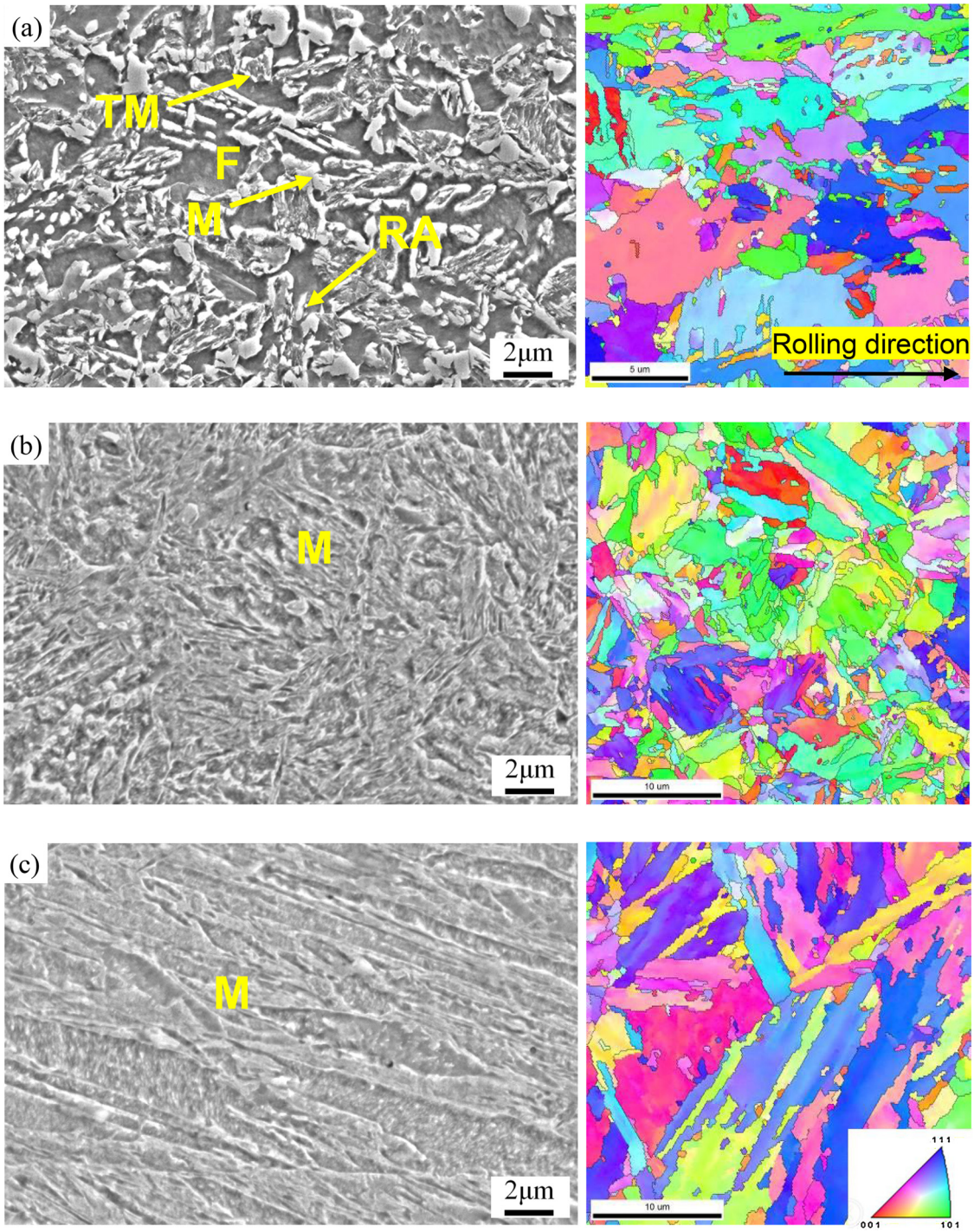

Fig. 5. SEM and inverse pole figure (IPF) with high angles of misorientation (θ > 15°): (a) BM QP980, (b) BM B1500HS and (c) FZ (F: ferrite; M: Martensite; RA: retained austenite).

marked with red color and, low angle boundaries with misorientation 2° < θ < 15°, and high angle boundaries with misorientation θ > 15°, were delineated by green and blue lines, respectively. The volume fractions of RA in BM and HAZ are shown in Table 2. It is noted that the volume fraction of RA in QP980 detected using EBSD was 8.4%, which was slightly lower than the value from XRD (10.8%). This difference may result from the tiny RA with grain size less than 0.05 μm, which were difficult to be detected using EBSD, as pointed out by Koopmans (2015). For example, Sun and Yu (2013) observed ~100 nm wide austenite films between martensite laths and ultrafine austenite films (20 ~ 30 nm in width) located between ferritic bainite plates in QP steels using transmission electron microscopy (TEM). EBSD showed that RA did not present in the super-critical HAZ of QP980 (Fig. 8b) but in the inter-critical HAZ and sub-critical HAZ (Fig. 8c and d). The QP980 and DP steel exhibited similar microstructure in inter-critical HAZs, where a small amount of RA (~0.6%) was observed. Yi

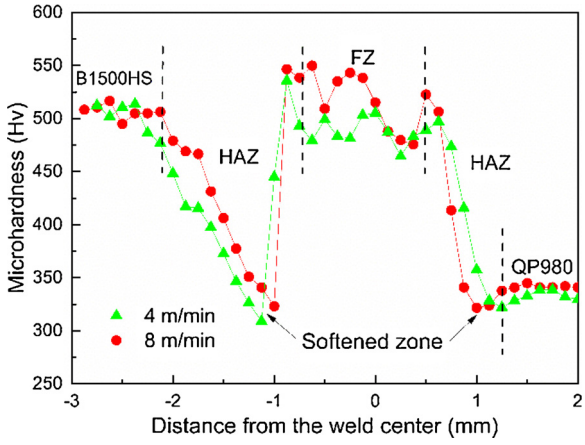

Fig. 6. Microhardness distribution across the welded joint.

et al. (1983) stated that the RA inevitably appeared in ferrite-martensite DP steels, and the content of RA increased with the temperature rising in the inter-critical range according to Bleck et al. (2004). In the sub-critical HAZ of QP980, the volume fraction of RA decreased to approximately 4.4% (Fig. 8d), as some of the RA could decompose into more stable phases such as ferrite and cementite due to the tempering effect, as reported by Zhou et al. (2012). The amount of RA left in HAZ after laser welding depended on its thermal stability. The decomposition of RA softened the material and impaired its enhanced mechanical properties as well in this study.

The B1500HS steel did not contain RA, as indicated in Figs. 4b and Figure 8e; however, after welding, approximately 0.9% and 3.4% volume fractions of RA formed in the super-critical and inter-critical HAZs, respectively (Table 2 and Fig. 8f and g). It should be noted that the super-critical and the inter-critical HAZs were extremely narrow (~375 μm); thus, the volume fraction of RA of the whole HAZ of B1500HS was too low to be detected by XRD.

Calcagnotto et al. (2010) reported that kernel average misorientation (KAM) could be used to express the geometrically necessary dislocations (GNDs) resulted from the phase transformation or rapid cooling during laser welding. The misorientation value up to 5° was calculated to avoid high KAM values along the grain boundaries based on the research by Khan et al. (2012). Fig. 9 shows the KAM maps of HAZ of QP980. It can be found that the martensite transformation induced GNDs existed within the martensite grains, while the ferrite grains presented low KAM. A considerable misorientation spread from martensite into ferrite through the phase boundaries in the inter-critical

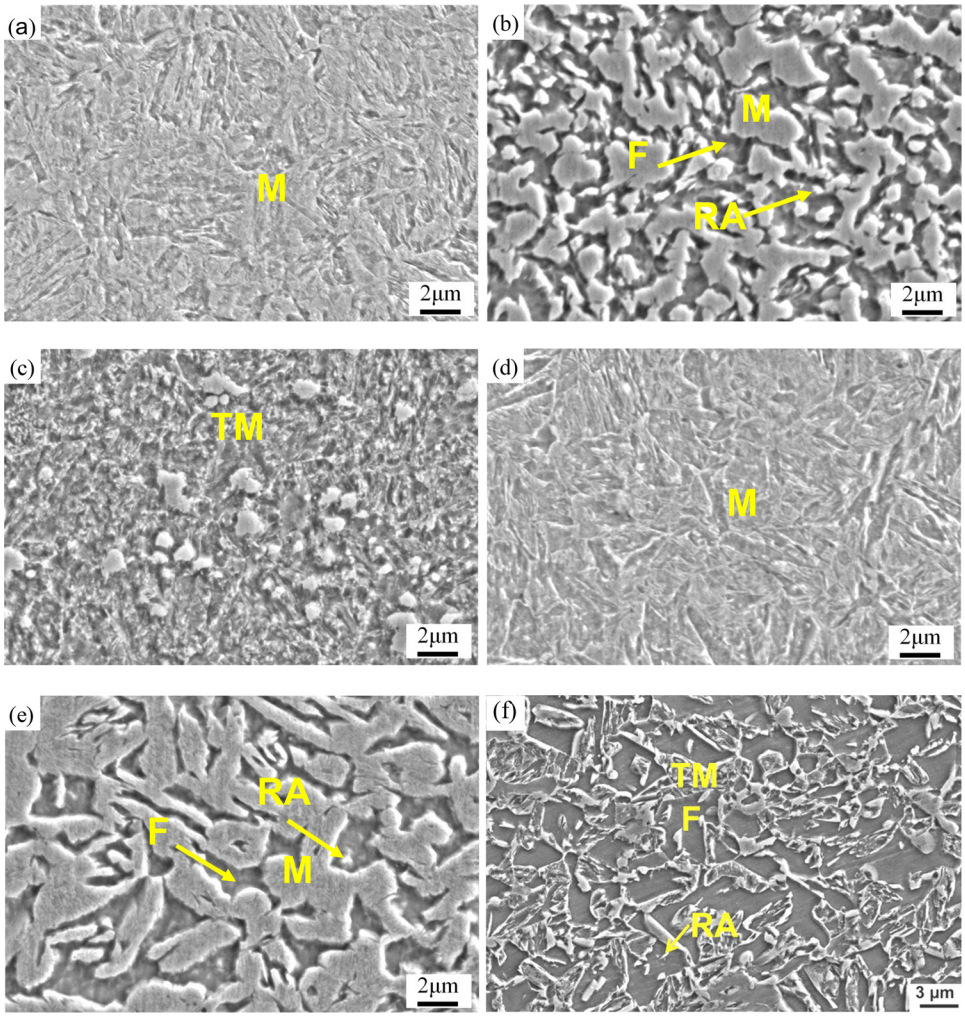

Fig. 7. SEM microstructure of HAZ welded at 8 m/min: B1500HS of (a) super-critical HAZ, (b) inter-critical HAZ and (c) sub-critical HAZ; QP980 of (d) super-critical HAZ, (e) inter-critical HAZ and (f) sub-critical HAZ (M: martensite; F: ferrite; TM: tempered martensite; RA: retained austenite).

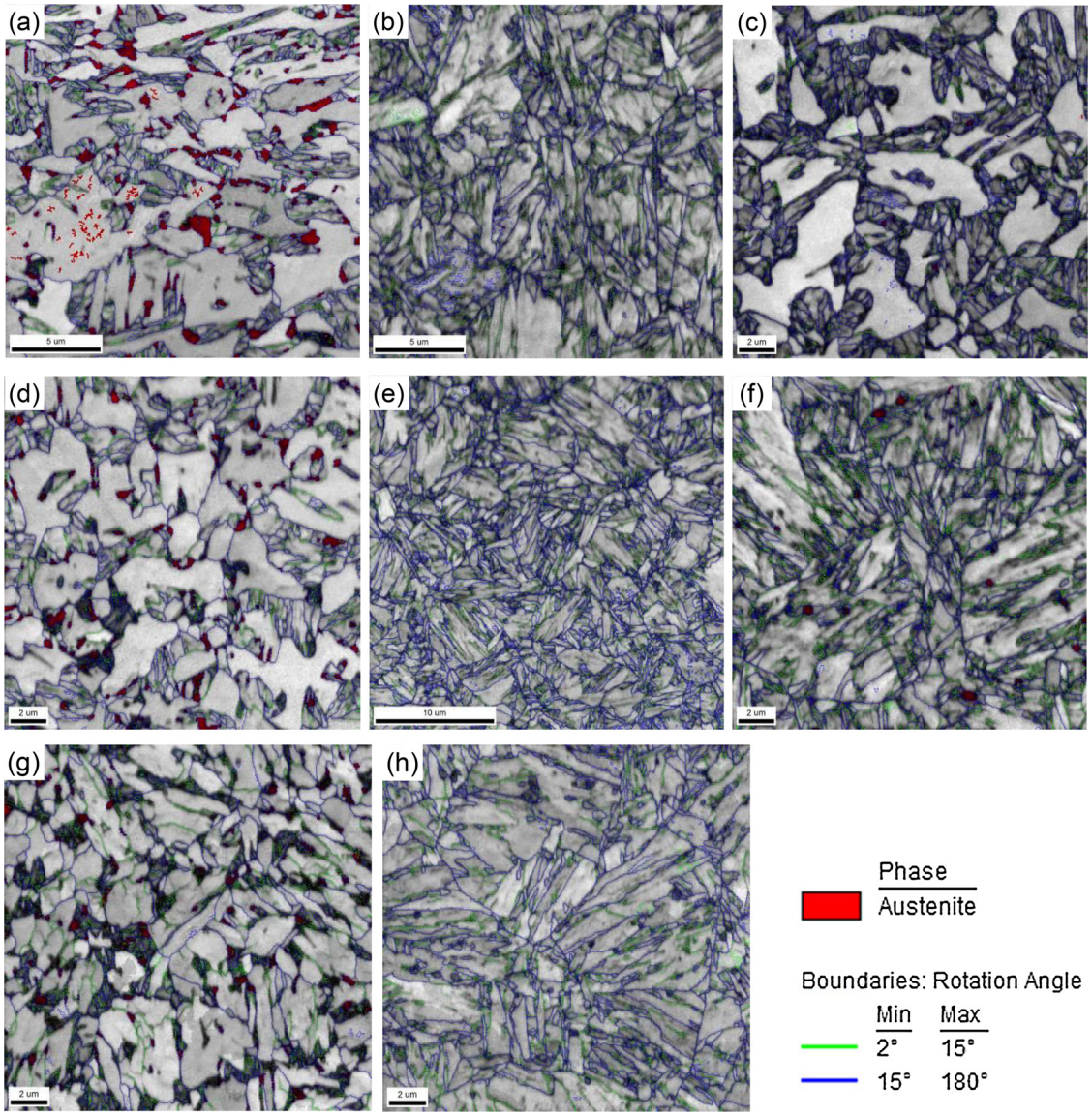

Fig. 8. Image quality (IQ) map with retained austenite: QP980 of (a) BM, (b) super-critical HAZ, (c) inter-critical HAZ and (d) sub-critical HAZ; B1500HS of (e) BM, (f) super-critical HAZ, (g) inter-critical HAZ and (h) sub-critical HAZ.

Table 2
Volume fraction of retained austenite (%).

	QP980				B1500HS			
Method	BM	Super-critical HAZ	Inter-critical HAZ	Sub-critical HAZ	BM	Super-critical HAZ	Inter-critical HAZ	Sub-critical HAZ
XRD	10.8	5.8			~0	~0		
EBSD	8.4	~0	0.6	4.4	~0	0.9	3.4	~0

HAZ of QP980, as shown in Fig. 9b, causing the ferrite work-hardening. This was induced by the volume expansion during the transformation of austenite to martensite, as reported by Bhattacharya (2014). When the HAZ experienced a temperature lower than A_{c1}, such as the sub-critical HAZ of QP980 in Fig. 9c, the misorientation gradients was significantly lowered and homogenized with the decomposition of martensite. Overall, the density of GNDs decreased from the super-critical HAZ to the sub-critical HAZ in QP980 side. These GNDs contribute to the stored energy and strain hardening during cold working, as described by Konijnenberg et al. (2015). As a result, the microhardness variation across the HAZ of QP980 exhibited similar decreasing trend to that of the GNDs, and the sub-critical HAZ was softened with lower micro-hardness than the BM (Fig. 6).

3.2. Mechanical properties

Tensile performance of BM and welded joints are presented in Fig. 10. The representative engineering stress-strain curves in Fig. 10a indicate that QP980 owned good ductility (26.1%) while B1500HS had ultra-high ultimate tensile strength (UTS,1587 MPa). For the dissimilar welded joints, the stress-strain curves exhibited high elongation when the joint failed at BM QP980 (Fig. 10b). This result was owing to the RA in the BM QP980 which progressively transformed into martensite under loading, leading to high work hardening rate, as indicated by Furnémont et al. (2002) and Jacques et al. (2001). However, the joints

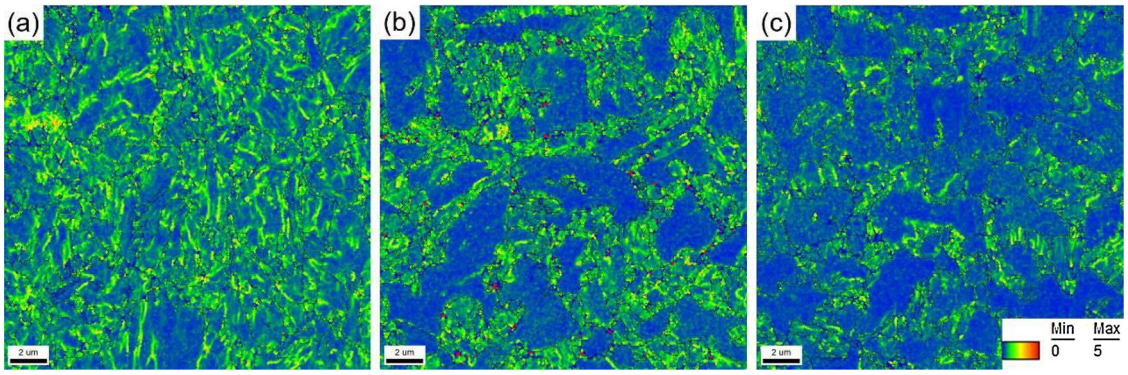

Fig. 9. KAM map (black line represents θ > 15°) of QP980 welded at 8 m/min: (a) super-critical HAZ, (b) inter-critical HAZ and (c) sub-critical HAZ.

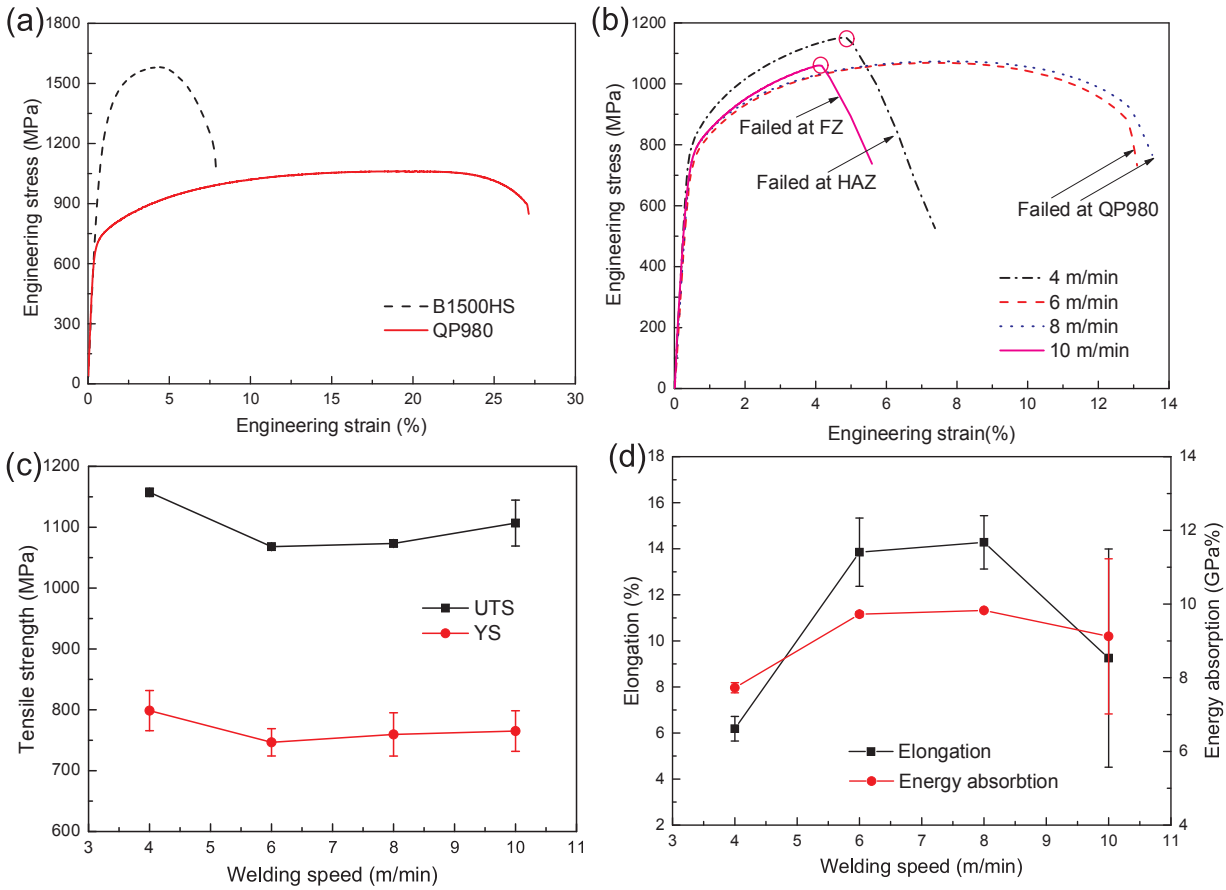

Fig. 10. Tensile properties of BM and welded joint: representative engineering stress-strain curves of (a) BM and (b) welded joint; (c) tensile strength of welded joint; (d) elongation and energy absorption of welded joint.

failed at HAZ or FZ presented low plasticity. Where the tensile fracture occurs depends on the heat input of the laser welding. When the welding speed was 4 m/min, excessive heat input brought about a high degree of HAZ softening in B1500HS, and consequently, the joint failed at the softened region. The welded joint presented the highest UTS of 1157 MPa but the lowest elongation of 6.2% (Fig. 10c and d). When the welding speed increased to 6 ~ 8 m/min, the softening degree of B1500HS was lowered, and the failure location transferred to BM QP980. Though the UTS slightly decreased to approximately 1070 MPa, the elongation increased to approximately 14.0%. An incompletely fused weld formed when the welding speed reached 10 m/min. In the case, the imperfect FZ became the failure location during tensile test, with a large decrease in the elongation to 9.1% and a slight increase in UTS to 1107 MPa. The yield strength (YS) showed a similar trend to the UTS at different welding speeds (Fig. 10c).

Energy absorption was calculated using the area below the stress strain curves up to 10% strain. With the welding speed varying from 4 to 10 m/min, the energy absorption increased to approximately 9.75 GPa% at 6 ~ 8 m/min, and then drastically decreased at 10 m/min. The joint welded at 10 m/min was not acceptable due to the incompletely fused weld, and the weld defect brought about great fluctuations in tensile properties (Fig. 10c and d). Despite the highest UTS

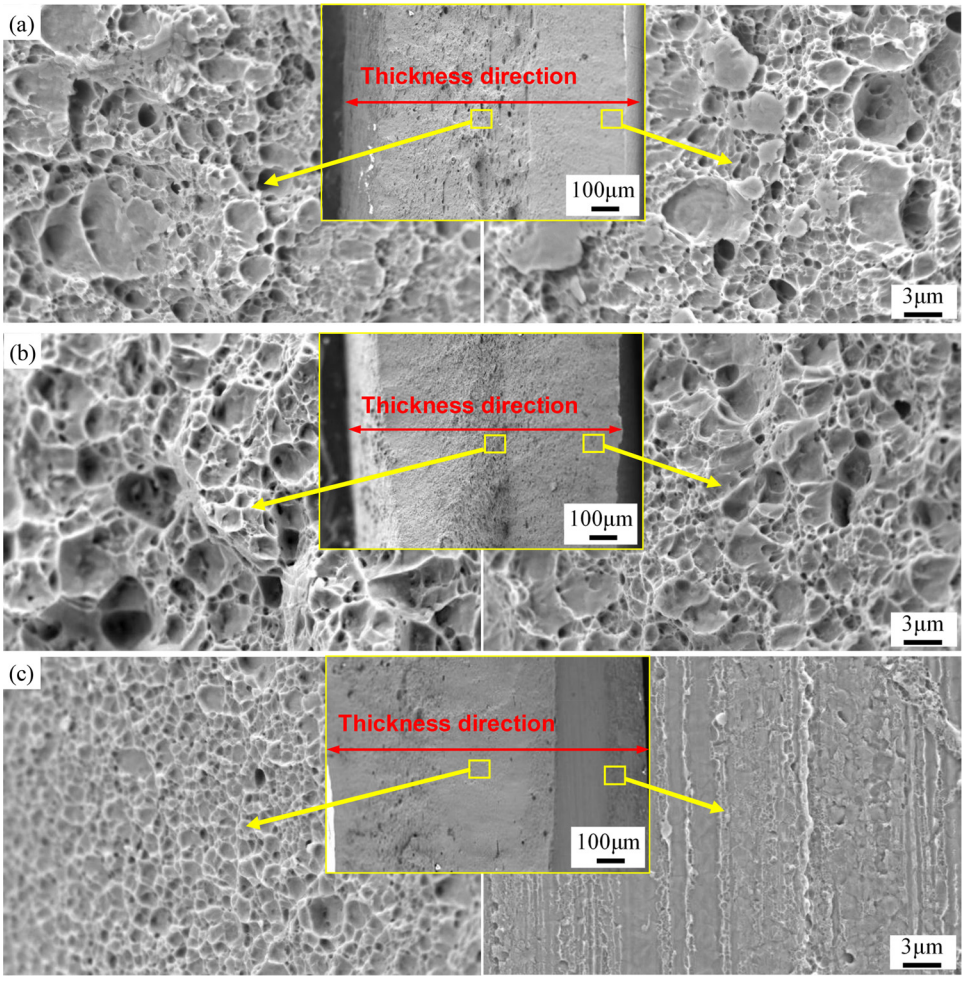

Fig. 11. Fracture surfaces of welded joint: (a) 4 m/min, (b) 8 m/min and (c) 10 m/min.

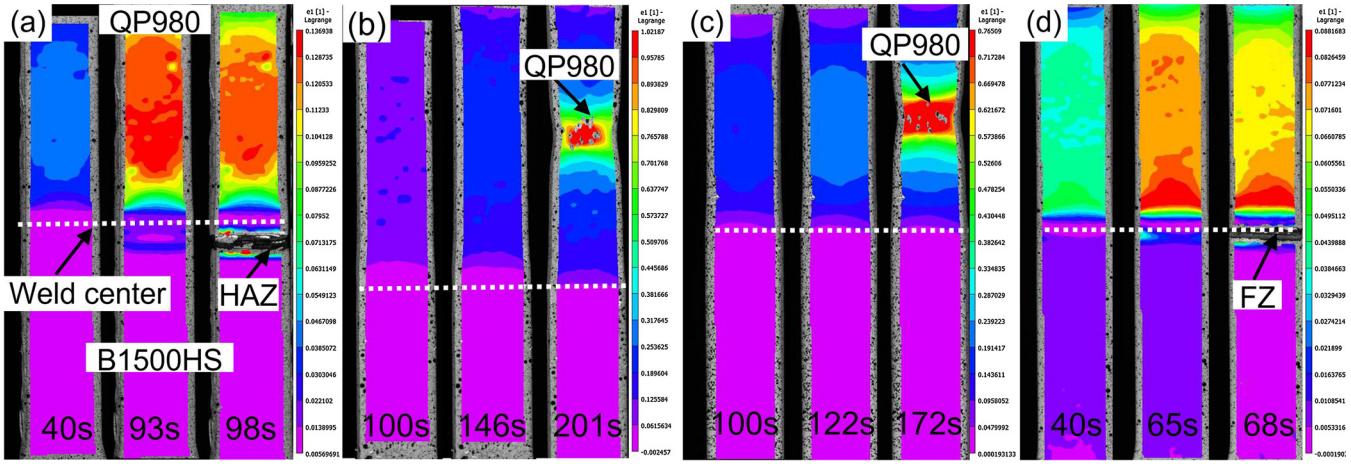

Fig. 12. DIC measurement of strain distribution during tensile loading showing three typical moments of uniform plastic deformation, peak load and start of failure: (a) 4 m/min, (b) 6 m/min, (c) 8 m/min and (d) 10 m/min.

of the welded joint at 4 m/min, the overall performance of welded joints at 6 ~ 8 m/min were more acceptable.

SEM fracture surfaces of the tensile samples are exhibited in Fig. 11. In Fig. 11a, the fracture surface of the joint welded at 4 m/min was featured by shallow dimples and quasi-cleavages. The fracture in mixed mode suggested the narrow softened HAZ of B1500HS still presented poor ductility. As illustrates in Fig. 11b, the joint (8 m/min) failed at QP980 were characterized by equiaxed and deep dimples at the middle area of the fracture surface and elongated dimples at the edge area, which was also observed by Farabi et al. (2010). The ductile fracture mode was desired, since large amounts of plastic deformation could absorb impact energy in a car crash. The ductile as well as cleavage patterns were observed on the fracture surface of the partially penetrated weld (10 m/min), as shown in Fig. 11c. The result showed that the weld experienced limited deformation before failure and the joint showed some brittle characteristic.

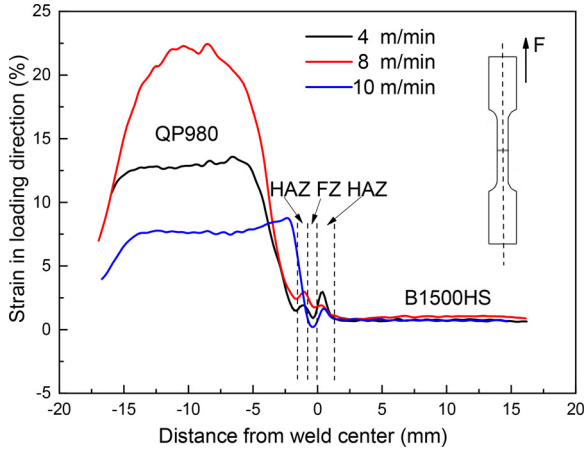

Fig. 13. Strain distribution under the maximum load in loading direction.

The strain distributions at three typical moments of uniform plastic deformation, peak load and start of failure were selected, as shown in Fig. 12. For all the dissimilar joints, the strain evenly distributed in BM QP980 in the uniform plastic deformation stage. However, with loading, the strain was localized in QP980, HAZ or FZ depending on the heat input.

Strain distribution in loading direction under the peak load is also displayed in Fig. 13 for comparison. It was found that the BM B1500HS of all joints under various heat inputs exhibited little deformation. The softened HAZ of B1500HS of the joint at 4 m/min exhibited the most significant strain localization as the load increased to the maximum value (Fig. 13). This was resulted from a high degree of martensite tempering in the HAZ under the large heat input, which led to HAZ softening. As a consequence, the deformation after peak load was confined at this region and the joint finally necked at the softened HAZ, as reported by Baltazar Hernandez et al. (2011). The FZ hardened with full martensite was the region with the lowest strain across the joint (Fig. 13). As discussed in our previous works (Jia et al., 2016, 2017), the hardened FZ restrained the deformation of the softened HAZ and strengthened it. Actually, there is a competition between the BM QP980 with conventional work hardening and TRIP effect and the softened HAZ of B1500HS with constraint from hardened FZ. Where the deformation occurs and accumulates depends on the competition. As a result, under optimized welding processes, e.g., 8 m/min, the strain finally localized in the BM and necking occurred there, as shown in Fig. 12c. The FZ and softened HAZ of B1500HS underwent less deformation than the regions of other joints when the welding speed reached 10 m/min, (Fig. 13), as there was weld defect in the FZ and the degree of HAZ softening was also much lower. This was in consistent with the fracture characteristic.

Formability of BMs and the welded joints without defects (4 ~ 8 m/min) were evaluated by Erichsen value and the load-displacement curves are illustrated in Fig. 14a. The Erichsen values of the welded joints, at the welding speed range of 4 ~ 8 m/min were comparable (~ 4.06 mm), as shown in Fig. 14b. However, the values were much lower than that of the BM B1500HS (7.46 mm) and QP980 steel (8.67 mm). It should be noted that all the welded joints made with various welding speeds failed at the softened HAZ of B1500HS during Erichsen tests, while the failure location of tensile test samples was dependent on heat input. The possible reason was that during Erichsen tests, the whole welded sample was under biaxial tensile stress state, and the strengthening effect of softened HAZ under uniaxial tension loading weakened. Thus the softened HAZ with the lowest hardness became the weakest region during biaxial stretch forming tests. The plastic deformation localized at the narrow softened HAZ of B1500HS, and the crack initiated and propagated there. As a result, the formability of the dissimilar joints significantly decreased compared with BM. Sreenivasan et al., (2008) also observed a large reduction in the formability of welded joint due to HAZ softening.

4. Conclusions

(1) QP980 and B1500HS steels have been successfully butt welded by fiber laser welding at a constant laser power 4.5 kW and various welding speeds of 4 ~ 8 m/min. Incomplete fusion of welds occurred at 10 m/min. For the joint welded at 8 m/min, the hardness of the softened HAZ of B1500HS significantly decreased by 187 Hv, while the hardness of the HAZ of QP980 merely dropped by 15 Hv.

(2) For the joint welded at 8 m/min, retained austenite was found in the super-critical HAZ of B1500HS (0.9%), inter-critical HAZ of B1500HS (3.4%) and inter-critical HAZ of QP980 (0.6%). The sub-critical HAZ of QP980 witnessed reduction of retained austenite from 8.4% to 4.4% because of decomposition during welding.

(3) The joints welded at 4 m/min achieved the highest UTS (1157 MPa) and YS (799 MPa), and the softened HAZ of the B1500HS was the weakest region. The dissimilar joint failed at BM QP980 at 6 ~ 8 m/min. The joints welded at 6 ~ 8 m/min were preferred as more crash energy can be absorbed.

(4) DIC measurement indicated that the strain evenly distributed in BM QP980 in the uniform plastic deformation stage of all the joints. As the load increased to the peak value, the hardened FZ experienced

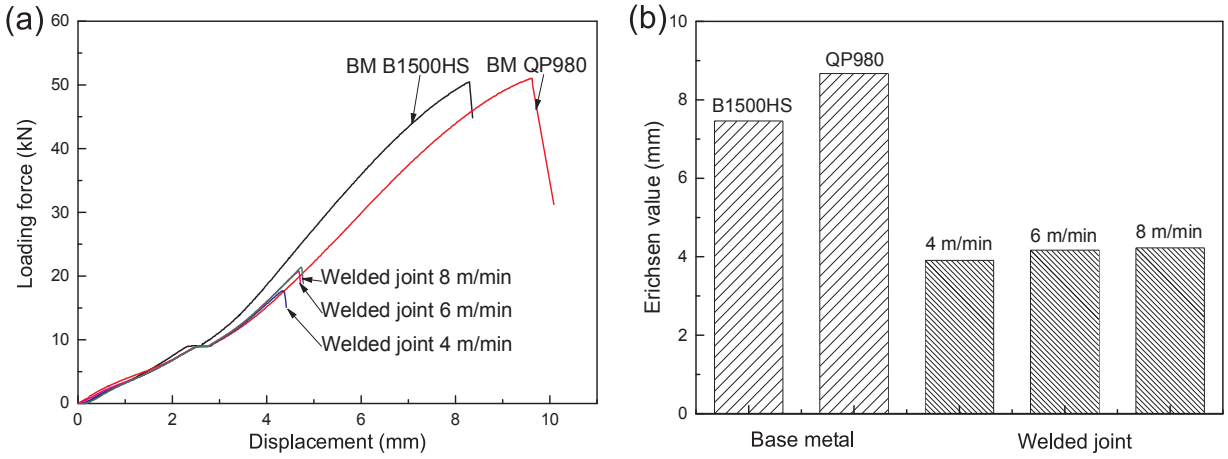

Fig. 14. Erichsen test results of BM and welded joint: (a) load-displacement curves and (b) Erichsen values.

less deformation and presented strain valley, while the softened HAZ deformed easily with different extent depending on the heat input.

(5) Erichsen test samples of the welded joints failed at the softened HAZ of B1500HS steel, and the Erichsen values (~4.06 mm) significantly decreased compared with that of BM B1500HS (7.46 mm) and QP980 steel (8.67 mm).

Declarations of interest

None.

Acknowledgements

This work was supported by the International Science and Technology Cooperation Program of China (No. 2015DFA51460) and National Natural Science Foundation of China (No. 51520105007).

References

Baltazar Hernandez, V.H., Nayak, S.S., Zhou, Y., 2011. Tempering of martensite in dual-phase steels and its effects on softening behavior. Metall. Mater. Trans. A 42, 3115–3129.

Bhattacharya, D., 2014. Microalloyed steels for the automotive industry. Tecnol. Metal. Mater. Miner. 11, 371–383.

Bleck, W., Papaefthymiou, S., Frehn, A., 2004. Microstructure and tensile properties in dual phase and trip steels. Steel Res. Int. 75, 704–710.

Calcagnotto, M., Ponge, D., Demir, E., Raabe, D., 2010. Orientation gradients and geometrically necessary dislocations in ultrafine grained dual-phase steels studied by 2D and 3D EBSD. Mater. Sci. Eng. A 527, 2738–2746.

Coates, G., 2014. Advanced High-Strength Steels Application Guidelines. World Auto Steel.

de Diego-Calderon, I., De Knijf, D., Monclus, M.A., Molina-Aldareguia, J.M., Sabirov, I., Foejer, C., Petrov, R.H., 2015. Global and local deformation behavior and mechanical properties of individual phases in a quenched and partitioned steel. Mater. Sci. Eng. A 630, 27–35.

Farabi, N., Chen, D.L., Li, J., Zhou, Y., Dong, S.J., 2010. Microstructure and mechanical properties of laser welded DP600 steel joints. Mater. Sci. Eng. A 527, 1215–1222.

Furnémont, Q., Kempf, M., Jacques, P.J., Göken, M., Delannay, F., 2002. On the measurement of the nanohardness of the constitutive phases of TRIP-assisted multiphase steels. Mater. Sci. Eng. A 328, 26–32.

Gu, Z., Yu, S., Han, L., Li, X., Xu, H., 2012. Influence of welding speed on microstructures and properties of ultra-high strength steel sheets in laser welding. ISIJ Int. 52, 483–487.

Jacques, P., Furnémont, Q., Pardoen, T., Delannay, F., 2001. On the role of martensitic transformation on damage and cracking resistance in TRIP-assisted multiphase steels. Acta Mater. 49, 139–152.

Jia, Q., Guo, W., Li, W., Zhu, Y., Peng, P., Zou, G., 2016. Microstructure and tensile behavior of fiber laser-welded blanks of DP600 and DP980 steels. J. Mater. Process. Technol. 236, 73–83.

Jia, Q., Guo, W., Li, W., Peng, P., Zhu, Y., Zou, G., Peng, Y., Tian, Z., 2017. Experimental and numerical study on local mechanical properties and failure analysis of laser welded DP980 steels. Mater. Sci. Eng. A 680, 378–387.

Jong, Y., Lee, Y., Kim, D., Kang, M., Hwang, I., Lee, W., 2011. Microstructural evolution and mechanical properties of resistance spot welded ultra high strength steel containing boron. Mater. Trans. 52, 1330–1333.

Khan, A.S., Baig, M., Choi, S., Yang, H., Sun, X., 2012. Quasi-static and dynamic responses of advanced high strength steels: experiments and modeling. Int. J. Plasticity 30-31, 1–17.

Konijnenberg, P.J., Zaefferer, S., Raabe, D., 2015. Assessment of geometrically necessary dislocation levels derived by 3D EBSD. Acta Mater. 99, 402–414.

Koopmans, T.T.W., 2015. Thermal Stability of Retained Austenite in Quenching & Partitioning Steels.

Lee, J.H., Park, S.H., Kwon, H.S., Kim, G.S., Lee, C.S., 2014. Laser, tungsten inert gas, and metal active gas welding of DP780 steel: comparison of hardness, tensile properties and fatigue resistance. Mater. Des. 64, 559–565.

Luo, X., Ren, J., Li, D., Qin, Y., Xu, P., 2016. Macro characteristics of dissimilar high strength steel resistance spot welding joint. Int. J. Adv. Manuf. Technol. 87, 1105–1113.

Nayak, S.S., Baltazar Hernandez, V.H., Okita, Y., Zhou, Y., 2012. Microstructure–hardness relationship in the fusion zone of TRIP steel welds. Mater. Sci. Eng. A 551, 73–81.

Němeček, S., Mužík, T., Míšek, M., 2012. Differences between laser and arc welding of HSS steels. Phys. Procedia 39, 67–74.

Speer, J., Matlock, D.K., De Cooman, B.C., Schroth, J.G., 2003. Carbon partitioning into austenite after martensite transformation. Acta Mater. 51, 2611–2622.

Speer, J.G., Assução, F.C.R., Matlock, D.K., Edmonds, D.V., 2005. The "quenching and partitioning" process: background and recent progress. Mater. Res. 8, 417–423.

Spena, P.R., De Maddis, M., Lombardi, F., Rossini, M., 2016. Dissimilar resistance spot welding of Q&P and TWIP steel sheets. Mater. Manuf. Process. 31, 291–299.

Sreenivasan, N., Xia, M., Lawson, S., Zhou, Y., 2008. Effect of laser welding on formability of DP980 steel. J. Eng. Mater-T ASME 130.

Sun, J., Yu, H., 2013. Microstructure development and mechanical properties of quenching and partitioning (Q&P) steel and an incorporation of hot-dipping galvanization during Q&P process. Mater. Sci. Eng. A 586, 100–107.

Wang, C.Y., Li, L., Li, H.R., Qin, C.L., Zhao, H.Y., 2013. Effects of welding heat input on 22MnB5 steel with hot-dipping Al coating. Adv. Mater. Res. 690-693, 2574–2577.

Wang, B., Duan, Q.Q., Yao, G., Pang, J.C., Li, X.W., Wang, L., Zhang, Z.F., 2014. Investigation on fatigue fracture behaviors of spot welded Q&P980 steel. Int. J. Fatigue 66, 20–28.

Yi, J.J., Yu, K.J., Kim, I.S., Kim, S.J., 1983. Role of retained austenite on the deformation of an Fe-0.07C-1.8Mn-1.4Si dual-phase steel. Metall. Mater. Trans. A 14, 1497–1504.

Zhou, S., Zhang, K., Wang, Y., Gu, J.F., Rong, Y.H., 2012. The mechanism of high strength-ductility steel produced by a novel quenching-partitioning-tempering process and the mechanical stability of retained austenite at elevated temperatures. Metall. Mater. Trans. A 43A, 1026–1034.

Zhou, L., Li, Z.Y., Song, X.G., Tan, C.W., He, Z.Z., Huang, Y.X., Feng, J.C., 2017. Influence of laser offset on laser welding-brazing of Al/brass dissimilar alloys. J. Alloy Compd. 717, 78–92.